Published February 23, 2015

Special Section: Soil-Mediated Drivers of Coupled Biogeochemical and Hydrological Processes across Scales

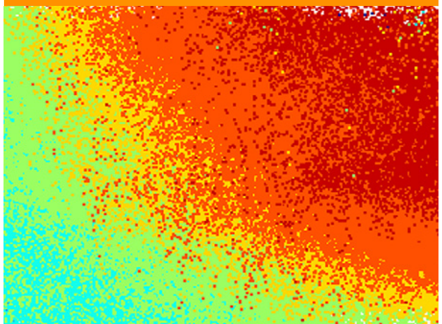

We have developed an improved method for measuring the transfer of energy and mass, in the form of water and carbon, to the subsurface critical zone. These transfers are fundamental to earth surface function and evolution.

C. Rasmussen, T.L. Swetnam, and J. Chorover, Dep. of Soil, Water and Environmental Science, Univ. of Arizona, Tucson, AZ 85719; J.D. Pelletier, Dep. of Geosciences, Univ. of Arizona, Tucson, AZ 85719; P.A. Troch, Dep. of Hydrology and Water Resources, Univ. of Arizona, Tucson, AZ 85719; and T.L. Swetnam, School of Natural Resources and the Environment, Univ. of Arizona, Tucson, AZ 85719. *Corresponding author (crasmuss@cals.arizona.edu).

Vadose Zone J.
doi:10.2136/vzj2014.07.0102
Received 31 July 2014.
Accepted 19 Nov. 2014.
Supplemental material online.

Quantifying Topographic and Vegetation Effects on the Transfer of Energy and Mass to the Critical Zone

Craig Rasmussen,* Jon D. Pelletier, Peter A. Troch, Tyson L. Swetnam, and Jon Chorover

Critical zone evolution, structure, and function are driven by energy and mass fluxes into and through the terrestrial subsurface. We have developed an approach to quantifying the effective energy and mass transfer (EEMT, MJ m^{-2} yr^{-1}) to the subsurface that accounts for local variations in topography, water and energy balances, and primary production. Our objectives were to quantify how (i) local topography controls coupled energy and water transfer to the subsurface, and (ii) vegetation effects on local-scale evapotranspiration and primary production controls of energy and mass transfer to the critical zone, both at the pedon- to hillslope-scale resolution, in the context of quantifying controls on EEMT. The model was tested across a semiarid environmental gradient in southern Arizona, spanning desert scrub to mixed conifer ecosystems. Data indicated clear variations in EEMT by topography, via both aspect and local water redistribution, and with current vegetative cover. Key findings include: (i) greater values of EEMT on north-facing slopes in a given elevation zone, with a north-facing aspect equivalent to an ~300-m elevation gain; (ii) a power law relationship between aboveground biomass and EEMT, with disturbance in the form of stand-replacing wildfire substantially reducing estimates of EEMT; and (iii) improved correlation of EEMT to pedon-scale variations in critical zone structure with EEMT values that include topography. Incorporating greater levels of environmental variation and complexity presents an improved approach to estimating the transfer of energy and mass to the subsurface, which is important to our understanding of critical zone structure and function.

Abbreviations: AET, actual evapotranspiration; CZ, critical zone; DEM, digital elevation model; EEMT, effective energy and mass transfer; LAI, leaf area index; MCWI, mass conservative wetness index; NAIP, National Agriculture Imagery Program; NPP, net primary production; PET, potential evapotranspiration; PPT, precipitation; SCM, Santa Catalina Mountains.

The evolution, structure, and function of the critical zone (CZ), the zone that extends from the top of the canopy down to the groundwater, is driven by energy and mass fluxes into and through the terrestrial subsurface. Internal fluxes and spatial structure coevolve in response to the transfer and transformation of energy and mass through the CZ system. Quantifying these fluxes is central to understanding CZ evolution and function at both short (10^{-3}– 10^{2} yr) and long (10^{3}– 10^{6} yr) time scales and to predicting the ability of the CZ to provide key services to society. Flux quantification represents a major challenge to CZ science (National Research Council, 2010), with a particular challenge in quantifying the relative importance of the influxes of water, C, radiation, etc., on driving CZ evolution and function. Placing these CZ influxes into the common currency of energy per unit area per unit time has shown significant promise in addressing this challenge across relatively "simple" landscapes, i.e., ignoring the complexities that local variations in topography and vegetation structure introduce into energy and mass influxes to the CZ. In this study, we further developed an energy metric approach to account for topographic and vegetation controls on CZ energy and mass influxes at pedon- to hillslope-scale (e.g., 10 m pixel^{-1}) resolution.

Recent work quantifying the transfer of energy and mass to the CZ via C derived from net primary production and water in excess of evapotranspiration indicates that these relatively simple-to-derive terms exhibit strong correlations with a range of CZ structural and functional properties (Rasmussen et al., 2011). The transfer term is referred to as "effective energy and mass transfer" (EEMT) because, while the C and water terms approximate only a fraction of the total energy and mass balance of CZ systems, these fluxes are deemed highly relevant to predicting subsurface physical, chemical, and biological properties. The previous applications of EEMT have largely been derived using relatively coarse-resolution temperature and precipitation data and temperature-based estimates of evapotranspiration that do not account for topographic and vegetative controls on local-scale water partitioning and primary production (Rasmussen, 2012; Rasmussen and Gallo, 2013; Rasmussen et al., 2005; Rasmussen and Tabor, 2007). This technique works well at regional scales and for describing broad patterns of CZ local development when arrayed across a large climate space. However, to accurately model catchment- to hillslope-scale EEMT, local topographic and vegetative factors controlling energy, water, and C transfer (including lateral fluxes) must be incorporated. For example, it is widely recognized across earth science disciplines that significant differences in water availability and hence CZ structure often occur on north- vs. south-facing hillslopes within the same region and elevation, particularly in water-limited environments (Broxton et al., 2009; Gutierrez-Jurado and Vivoni, 2013; Melton, 1960; Pelletier et al., 2013; Poulos et al., 2012). Previous methods for computing EEMT did not adequately honor such local, microclimatic variations. The empirical model for calculating EEMT presented by Chorover et al. (2011) used vapor pressure deficit and topographically modified temperature as a means to introduce topographic controls on local EEMT rates; however, this formulation was purely correlative and did not include theory grounded approximations of topographic effects on pedon- to hillslope-scale water, energy, and C balances.

This study addressed the overarching question of how topography and vegetation affect local-scale estimates of EEMT. Our objective, therefore, was to develop a methodology for calculating how (i) local topography controls coupled energy and water balances and (ii) vegetation affects local-scale evapotranspiration and primary production and how this variation affects estimates of EEMT. Unique sets of values for EEMT that incorporate varying levels of topographic and vegetation information were then compared with a simple metric of CZ structure—soil depth—to demonstrate the relative improvement in the relationship between EEMT and pedon- to hillslope-scale CZ structural variation imparted by incorporation of greater topographic complexity into the EEMT framework. The EEMT framework applied here is just one specific approach for quantifying energy and mass transfer to the CZ, but the use of solar radiation to modify the local temperature and vapor pressure deficit along with topographic controls on water redistribution are central and relevant to any effort to quantify how topography influences CZ energy and water availability.

Conceptual Framework

The EEMT framework is built around the premise that CZ processes and evolution are a direct function of gradient-driven fluxes of energy and mass, including solar radiation, C, water, and the mineral or sediment supply. Cycling and storage of energy and mass occurs through processes such as infiltration and recharge, primary production and C cycling, physical and chemical weathering, and erosion and sediment transport. Export of energy and mass occurs through evapotranspiration, CO_2 respiration, runoff and base flow, and denudation (Fig. 1). The CZ may thus be conceptualized to function as an open thermodynamic system wherein the flux of energy and mass into and through the system drives internal cycling processes that result in the formation of organized structures. These structures optimize energy and mass storage as well as system export of dissipative products. Quantifying the relevant influx of energy and mass provides a predictive capability

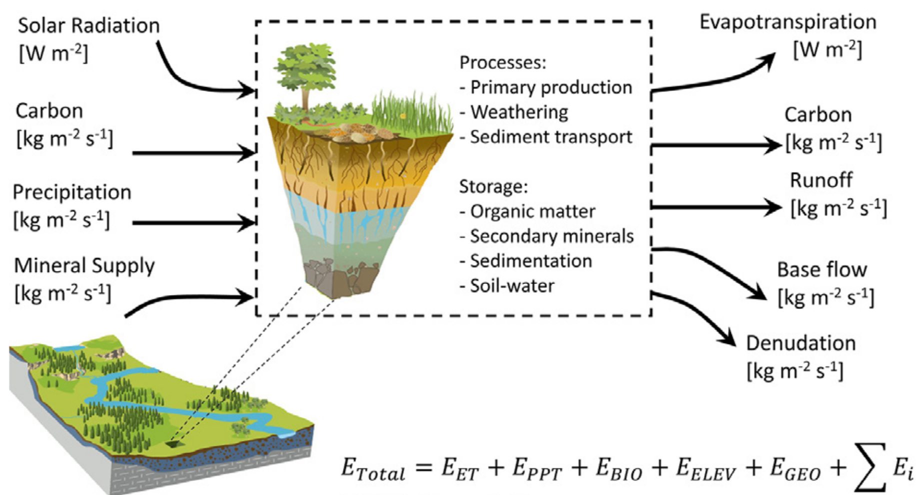

$$E_{Total} = E_{ET} + E_{PPT} + E_{BIO} + E_{ELEV} + E_{GEO} + \sum E_i$$
$$EEMT = E_{ePPT} + E_{BIO}$$

Fig. 1. Conceptual framework characterizing major fluxes and processes in the critical zone. The fluxes may be quantified in terms of energy and mass balance terms, with the total energy transferred to the critical zone (E_{Total}) the sum of energy associated with evapotranspiration (E_{ET}), precipitation (E_{PPT}), net primary production (E_{BIO}), erosion and sediment transport (E_{ELEV}), geochemical gradients (E_{GEO}), and any other energy and mass transfers E_i) Effective energy and mass transfer (EEMT) is equal to the net energy and mass fluxes associated with effective precipitation (E_{ePPT}) and net primary production (E_{BIO}) (modified from Rasmussen, 2012; artwork from Chorover et al., 2007).

for quantifying CZ processes and structural organization under the hypothesis that greater energy and mass flux results in greater structural organization and output of dissipative products (Rasmussen et al., 2011).

The EEMT framework was developed from the classic soil-forming factor approach (Jenny, 1941) that states that soil properties are a function of climate, biota, relief, parent material, and landscape age. Rasmussen (2012) restated this as: CZ = $f(T$, VPD, PPT, R_n, C, $S)t_r$, where CZ is the critical zone state, T is the temperature, VPD is the vapor pressure deficit, PPT is precipitation, R_n is net solar radiation, C is the carbon content, S is the mineral supply and sediment transport, and t_r is the relative age of the system, which explicitly links each factor with key CZ energy and mass balances. Volobuyev (1964) attempted to formalize these factors into quantitative energy terms and stated that soil properties could be equated to the summation of energy and mass fluxes associated with soil development, where *development* refers to chemical alteration, structure formation, and the layering, zonation, and organization of the weathered regolith. The summation of these fluxes was stated as (Minasny et al., 2008): $E = w_1 + w_2 + b_1 + b_2 + e_1 + e_2 + g + v$, where E is the energy involved in soil formation, w_1 is the energy of physical rock weathering, w_2 is the energy for chemical weathering, b_1 is the energy accumulating in the soil organic matter, b_2 is the energy for soil organic matter transformation, e_1 is the energy for evaporation from the soil surface, e_2 is the energy for transpiration, g is the energy losses in leaching of salts and fine materials, and v is the energy expended by the process of heat exchange between the soil and the atmosphere, generally negligible across the centurial to millennial time scales of soil formation.

Rasmussen et al. (2011) took a similar approach and derived this basic statement from the respective energy, water, C, and sediment balances that occur on the Earth's surface, including tectonically forced gravity-driven sediment transport, and the geochemical alteration of primary and secondary mineral phases (J m^{-2} s^{-1}), stated as

$$E_{\text{Total}} = E_{\text{ET}} + E_{\text{PPT}} + E_{\text{BIO}} + E_{\text{ELEV}} + E_{\text{GEO}} + \sum E_i \qquad [1]$$

where E_{ET} is the energy and mass flux associated with evapotranspiration, E_{PPT} is the heat energy associated with precipitation energy and mass transfer, E_{BIO} is the net primary productivity energy and mass transfer, E_{ELEV} is the potential energy associated with gravity-driven transport of sediment, E_{GEO} is the geochemical potential of chemical weathering, and E_i is any other external energy and mass input such as dust, anthropogenic inputs, or the heat exchange between the soil and the atmosphere. The E_{ET} term by far represents the largest component of E_{Total} and is typically several orders of magnitude greater than the sum of the remaining energy and mass flux terms (Phillips, 2009). However, given that E_{ET} represents the transfer of water and radiant energy back to the atmosphere, it has limited potential for performing chemical or physical work on the subsurface. Equation [1] may thus be restated in terms of energy and mass transferred to the subsurface ($E_{\text{Subsurface}}$, J m^{-2} s^{-1}):

$$E_{\text{Subsurface}} = E_{\text{ePPT}} + E_{\text{BIO}} + E_{\text{ELEV}} + E_{\text{GEO}} + \sum E_i \qquad [2]$$

where the precipitation term, E_{ePPT}, denotes effective precipitation, which accounts for precipitation water loss to evapotranspiration. As noted, the E_{ELEV} and E_{GEO} terms encompass the physical and chemical transfers of energy and mass associated with denudation and mineral transformation. In many Earth surface systems, the sum of these fluxes may be orders of magnitude less than the water and C flux terms (Phillips, 2009). Therefore, we have focused on the sum of energy and mass transfer associated with effective precipitation and primary production, which Rasmussen et al. (2011) referred to as *effective energy and mass transfer* (EEMT, J m^{-2} s^{-1}), defined as:

$$\text{EEMT} = E_{\text{ePPT}} + E_{\text{BIO}} \qquad [3]$$

where EEMT represents the summation of energy transferred to the subsurface CZ as the heat and mass transfer associated with effective precipitation (E_{ePPT}) and chemical energy associated with reduced C compounds derived from primary production (E_{BIO}).

The components of EEMT (Eq. [3]) have units of joules per square meter per second or watts per square meter and may be calculated using relatively simple monthly water balance techniques (e.g., Arkley, 1963) and net primary production estimates (e.g., Lieth, 1975). The value of E_{ePPT} (J m^{-2} s^{-1}) is calculated as

$$E_{\text{ePPT}} = Fc_{\text{w}}\Delta T \qquad [4]$$

where F is the mass flux of water available to move into and through the subsurface (kg m^{-2} s^{-1}), c_{w} is the specific heat of water (J kg^{-1} K^{-1}), and $\Delta T = T_{\text{ambient}} - T_{\text{ref}}$ (K), with T_{ambient} the ambient temperature at the time of water flux and T_{ref} set at 273.15 K. The value of E_{BIO} (J m^{-2} s^{-1}) is calculated as

$$E_{\text{BIO}} = \text{NPP}\ h_{\text{BIO}} \qquad [5]$$

where NPP is the mass flux of C as net primary production (kg m^{-2} s^{-1}) and h_{BIO} is the specific biomass enthalpy (J kg^{-1}) fixed at a value of 22×10^6 J kg^{-1}.

For the purposes of this study, we calculated and compared EEMT derived using three different approaches that incorporated increasing levels of complexity and spatial patterns of topography and vegetation. The three methods were: (i) the "traditional" approach based on relatively simple energy and water balances and net primary production estimates (EEMT$_{\text{TRAD}}$); (ii) a modified approach that captures topographic controls on energy, water, and

C balances ($EEMT_{TOPO}$); and (iii) an approach that integrates both topographic controls on the water and energy balances and point-scale vegetation controls on surface resistance and primary production ($EEMT_{TOPO\text{-}VEG}$).

Methods

Study Area

The Sabino Creek watershed in the Santa Catalina Mountains (SCM) in southern Arizona, just outside of Tucson, served as the test area for model development and represents well the typical range of climate, vegetation, and soils associated with the Sky Islands of the Desert Southwest (Fig. 2 and 3). The watershed covers approximately 9100 ha and encompasses a steep elevation and, hence, environmental gradient that spans hot, dry, semiarid desert scrub ecosystems at elevations near 800 m asl to cool, subhumid, mixed conifer forests at high elevations, with a maximum elevation of ~2800 m asl. The underlying bedrock is dominated by Tertiary-aged granitic rocks at mid to upper elevations and Tertiary-aged mylonite, a metamorphosed granitic gneiss, at low to mid elevations, with sparse cover of Paleozoic metasedimentary rocks at the highest elevations (Dickinson, 1992). Soils exhibit minimal soil development across the gradient, with the greatest differences being a trend from shallow (<50 cm to saprock) to moderately deep (100–150 cm to saprock) soils and increasing organic matter content with elevation (Lybrand et al., 2011; Pelletier et al., 2013; Whittaker et al., 1968).

Mean annual temperature decreases from near 22°C at low elevations to a minimum near 6 to 7°C at high elevation. Mean annual precipitation follows an inverse pattern, with the lowest precipitation amounts of 250 mm yr^{-1} at low elevation and an increase to near 800 mm yr^{-1} at high elevation (Fig. 3a and 3b). All elevations possess a bimodal precipitation regime, with an approximate 50:50 split between winter and summer precipitation. The high-elevation systems above ~2000 m receive much of the winter precipitation as snow; however, these systems are sufficiently warm during the winter that they do not typically maintain a deep seasonal snowpack, with winter climate patterns typified by pulses of snowfall and subsequent melt events (Heidbuchel et al., 2013).

Disturbance in the Sabino Creek watershed largely derives from wildfire events, with wildfire recognized as a major driver of CZ processes and development in the western United States (Dennison et al., 2014; Holden et al., 2012; Littell et al., 2009; Westerling et al., 2003). The Sabino Creek watershed has been subjected to a number of fires during the last several decades, the most significant of which was the Aspen fire in 2003 that burned >7880 ha in the watershed or roughly 87% of the catchment area (Magirl et al., 2007). Burn severity maps

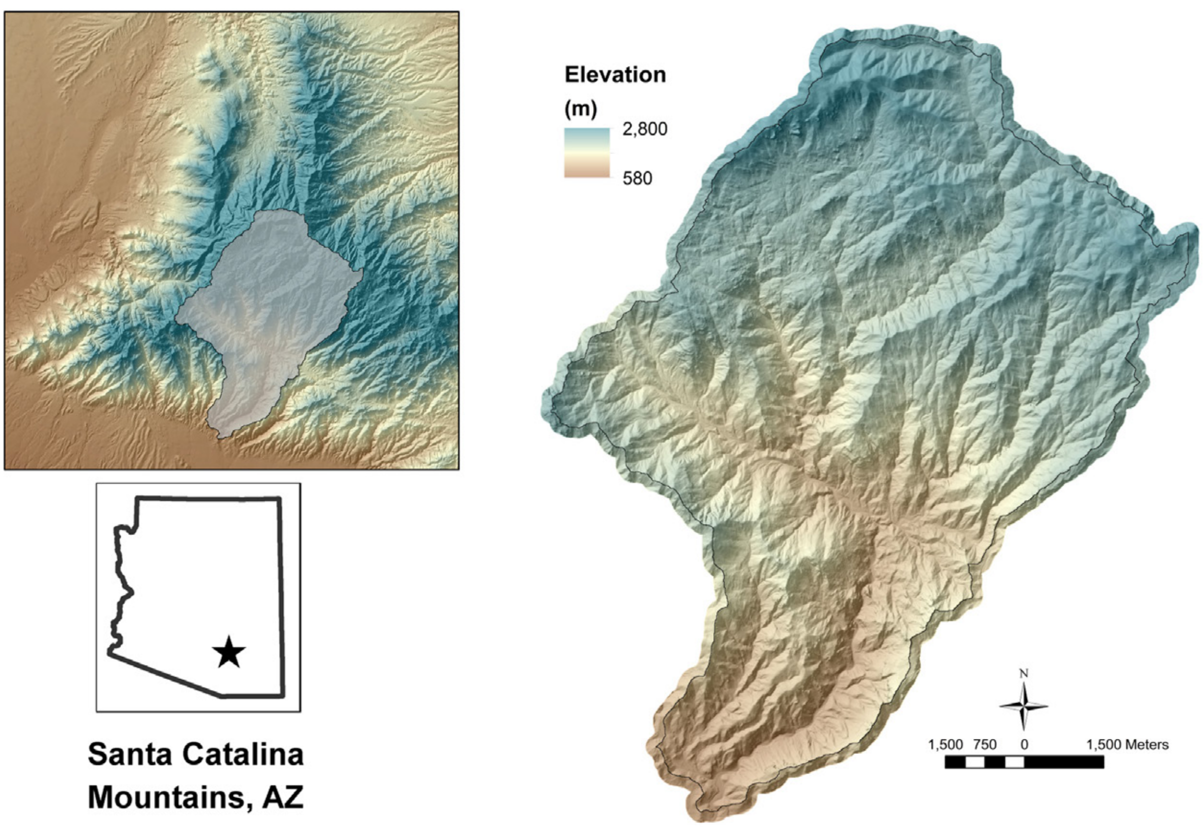

Fig. 2. Location of the Sabino Creek watershed in the Santa Catalina Mountains in southern Arizona. The watershed covers >9100 ha and spans an elevation gradient ranging from 580 m to 2800 m asl.

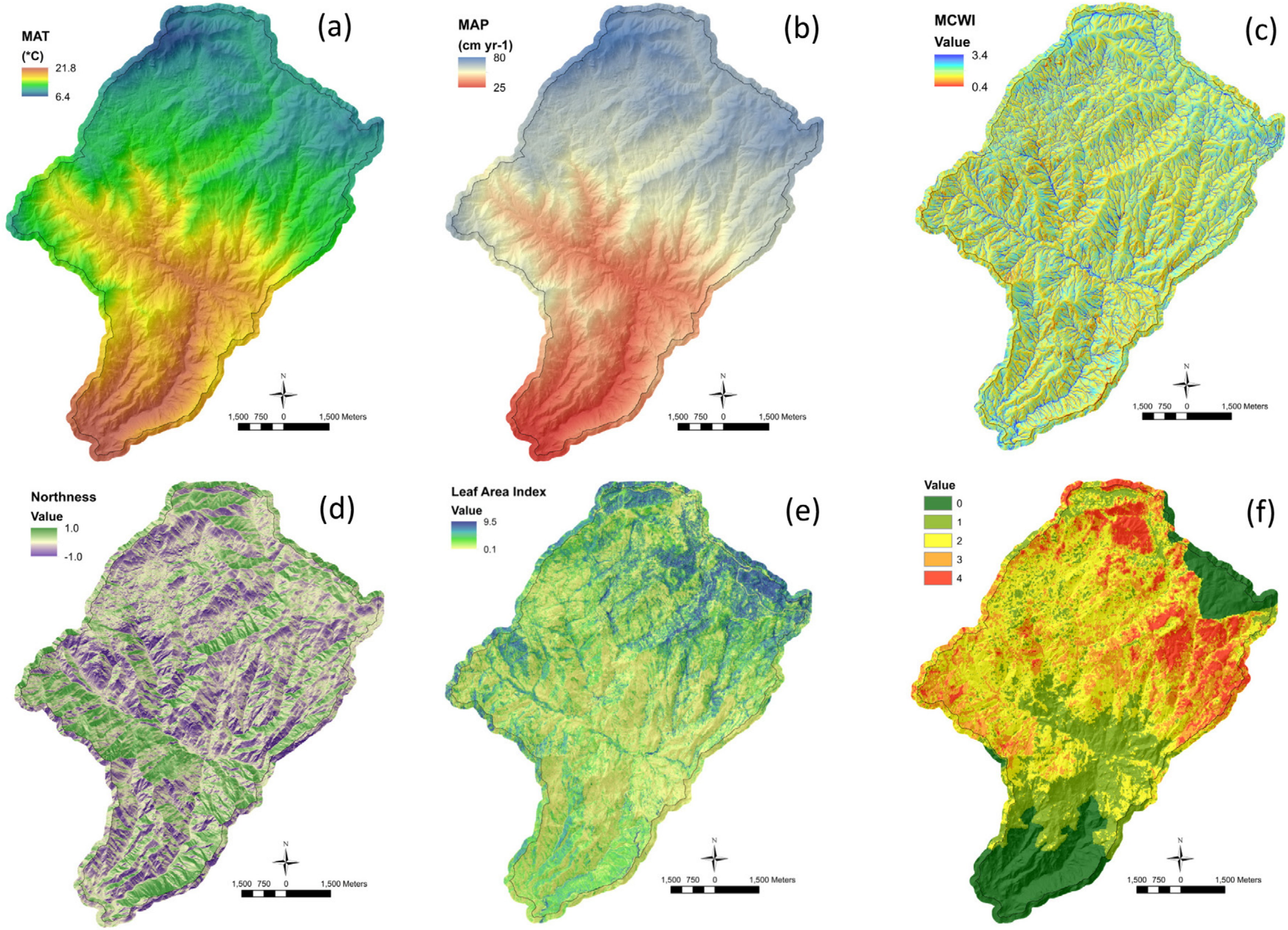

Fig. 3. Physiographic characteristics of the Sabino Creek watershed including (a) mean annual temperature (MAT) modeled based on topography and locally derived lapse rates, (b) mean annual precipitation (MAP) modeled based on local orographic rainfall patterns, (c) a mass conservative wetness index (MWCI) derived from slope and catchment areas, (d) northness as a proxy for aspect, (e) leaf area index (LAI) modeled from a local normalized difference vegetation index derived from a 2010 aerial photograph, and (f) burn severity resulting from the 2003 Aspen fire.

derived from pre- and post-burn LandSat imagery (http://www.fs.usda.gov/detail/r3/landmanagement/gis/?cid=stelprdb5208076) indicated only ∼760 ha of severe burn, or 8% of the catchment, with 3150 ha, or 35% of catchment area, of low severity to no burn (Fig. 3f). The levels of burn severity documented for the Aspen fire were used as a metric for characterizing disturbance effects on EEMT.

A high-resolution (1 m pixel^{-1} resolution) LiDAR data set (Pima Association of Governments, http://www.pagnet.org) for the SCM was used as the base set of elevation data for climate and topographic modeling. Data products extracted from the LiDAR data included both the bare earth digital elevation model (DEM) and canopy height. The LiDAR data were rescaled to a 10 m pixel^{-1} resolution to facilitate rapid computational processing across the relatively large study area.

The three methods for calculating EEMT included: (i) $\text{EEMT}_{\text{TRAD}}$ based on simple energy and water balances and net primary production estimates; (ii) $\text{EEMT}_{\text{TOPO}}$ that captures topographic controls on energy, water, and C balances; and (iii) $\text{EEMT}_{\text{TOPO-VEG}}$ that integrates both topographic controls on water and energy balances and vegetation controls on surface resistance and primary production. All of these calculations rely on a base set of climate, solar radiation, and leaf area index data. Evapotranspiration and net primary production for each method vary with: (i) $\text{EEMT}_{\text{TRAD}}$ relying on simple empirical approximations based on climate parameters; (ii) $\text{EEMT}_{\text{TOPO}}$ using a Penman–Monteith approach to estimate potential evapotranspiration coupled with a Budyko curve to approximate actual evapotranspiration and empirical estimates of primary production based on topography; and (iii) $\text{EEMT}_{\text{TOPO-VEG}}$ implementing a full Penman–Monteith approach to calculating actual evapotranspiration that includes pixel-based measures of surface and aerodynamic resistance and a canopy-height-based approximation of primary production. The parameters used for each approach are outlined below.

Local Climate, Solar Radiation, and Leaf Area Data

Local climate data were derived for a set of remote area weather stations managed by the US Forest Service (http://www.raws.dri.edu/). Data from three stations in the Santa Catalina Mountains and adjacent Rincon Mountains that span the full elevation gradient were processed for mean monthly minimum and maximum temperatures, precipitation, relative humidity, and wind speed. The three stations, Saguaro at 800 m asl, Soller Spring at 2300 m asl, and Rincon at 2512 m asl, have an average period of record of 12 yr, providing a reasonable climatological data set. Climate parameters including temperature, precipitation, relative humidity, and wind speed were regressed relative to elevation on a monthly basis, with most parameters exhibiting a linear relationship to elevation (Supplemental Fig. S1). These relationships were used to calculate mean monthly climatological norms for each 10-m pixel in the study area and served as the base climate data for the modeling detailed below.

Solar Radiation

Total incoming shortwave solar radiation (direct and diffuse) was calculated on a monthly basis using the 10-m DEM and the solar radiation routine in ArcGIS 10.0 that accounts for variations in latitude, elevation, and aspect. The applied algorithm does not account for topographic shielding and shadowing and thus may overestimate radiation in certain portions of the landscape, particularly those associated with south-facing convergent areas that may experience morning shading from adjacent north-facing slopes (Beaudette and O'Geen, 2009). Incoming radiation was calculated incorporating topographic variation in slope and aspect, S_{topo}, as well as for a free flat surface with constant values of zero for slope and aspect, S_{flat}. The ratio of the two, $S_i = S_{\text{topo}}/S_{\text{flat}}$, was used for modeling topographic modifications of temperature (see below). Calculations for both S_{topo} and S_{flat} were performed on a monthly basis using a 2-h time step, a sky view of 200 pixels, 32 calculation directions, eight zenith and azimuth divisions, and uniform clear sky conditions.

Leaf Area Index

A leaf area index (LAI) was derived using a vegetation index approach that predicts LAI using a remotely sensed normalized difference vegetation index (NDVI). The 1 m pixel^{-1} resolution National Agriculture Imagery Program (NAIP) four-band imagery data collected for all of Arizona in June of 2010 that included red, blue, green, and near-infrared (NIR) spectra was used as the base data for calculating NDVI and LAI. The NDVI was calculated from the NAIP NIR and red bands as (Huete et al., 1994) (NIR − Red)/(NIR + Red). The third-order polynomial function of Qi et al. (2000), derived for semiarid regions in southern Arizona, was used to calculate the LAI from the NDVI as $ax^3 + bx^2 + c + d$, where x is the NDVI and a, b, c, and d are 18.99, −15.24, 6.124, and −0.352, respectively. Calculated values for LAI ranged from 0 to 9.5 for the study area. The LAI data were calculated at a 1 m pixel^{-1} resolution, then resampled to the 10 m pixel^{-1} resolution of the DEM.

Modeled values for LAI increased from a minimum of 0.1 in low-elevation desert ecosystems to 9.5 in the high-elevation mixed conifer ecosystems (Fig. 3e). The highest values for each elevation occurred on north-facing slopes and in drainageways where topography controls the local energy and water balance and water available for primary production. The largest impacts of recent wildfire activity on the LAI were noted in the high-elevation conifer ecosystems that experienced a high-severity, stand-replacing burn.

Topographically Modified Temperature

Following Moore et al. (1993), minimum, maximum, and mean monthly air temperatures (°C) at each pixel (T_i) were calculated using the local lapse rate, topographically modified solar radiation (S_i), and LAI:

$$T_i = T_{\text{b}} - T_{\text{lapse}}\left(\frac{z_i - z_{\text{b}}}{1000}\right) + C\left(S_i - \frac{1}{S_i}\right)\left(1 - \frac{\text{LAI}_i}{\text{LAI}_{\max}}\right) \qquad [6]$$

where T_b is the temperature (°C) at a base station; T_{lapse} is the local lapse rate (°C km^{-1}); z_i and z_b are the elevation (m) of the pixel and base station, respectively; C is a constant equal to 1; S_i is the ratio between direct shortwave radiation on the actual surface and direct shortwave radiation on a horizontal surface; LAI_i is the pixel leaf area index; and LAI_{max} is the maximum value for LAI, equal to 10.

The mean monthly minimum and maximum temperatures (T_{min} and T_{max}) were calculated using the monthly minimum and maximum temperature lapse rates derived from the climate station and elevation data. The low-elevation station was selected as the base station for determining both T_b and z_b. The minimum temperature was calculated using only the minimum temperature lapse rate, i.e., ignoring the second term in Eq. [6], because minimum temperatures occur at night when there is a negligible effect of solar radiation or LAI on the temperature. The mean monthly temperature was calculated as the average of T_{min} and T_{max}.

The amount of information included in the temperature calculations varied with each EEMT modeling approach. Specifically, $EEMT_{TRAD}$ used temperature calculated using only the derived lapse rates; $EEMT_{TOPO}$ incorporated the solar radiation term but did not include LAI; and $EEMT_{TOPO\text{-}VEG}$ included all terms in Eq. [6].

Local Water Balance

The wetting of each pixel per month was approximated using a local water balance (L'vovich, 1979):

$$W = PPT - SR = AET + F \qquad [7]$$

where W is pixel wetting (m s^{-1}), PPT is the mean annual precipitation, SR is surface runoff, AET is actual evapotranspiration, and F is the water partitioned to base flow. The F term quantifies subsurface wetting, a key parameter for calculating EEMT (see below), and represents the fraction of water with the ability to transfer heat energy and perform chemical and physical work in the subsurface. Equation [7] may be rewritten to solve for F as $F = P_{eff} - SR$, where P_{eff} is the effective precipitation, equivalent to PPT − AET. Effective precipitation is thus a key component of the water balance approach applied here and central to calculating EEMT. The three approaches to modeling EEMT varied in the calculation of P_{eff} and specifically the calculation of the AET term, as described below. The length scale of precipitation and evapotranspiration were scaled to units of mass per unit area per unit time based on the density of water and the assumption that a meter of precipitation is equivalent to 1 m^3 H_2O m^{-2}.

Evapotranspiration for Traditional Effective Energy and Mass Transfer

We applied three techniques for calculating the actual evapotranspiration that incorporate various levels of detail of environmental data. The original formulation of EEMT (Rasmussen et al., 2005) relied on a very simple water balance approach commonly used in pedologic studies wherein P_{eff} was determined as the difference between monthly precipitation and potential evapotranspiration (PET) calculated using the Thornthwaite and Mather (1957) temperature-based approach. In the calculation of $EEMT_{TRAD}$ in this study, we calculated PET using Hamon's equation (PET_H) that incorporates temperature, daylight, and saturated vapor pressure (see Supplemental Material) and provided values nearly identical to the Thornthwaite–Mather approach across the study area (Haith and Shoemaker, 1987; Hamon, 1961).

Evapotranspiration for Topographically Modified Effective Energy and Mass Transfer

The modeling approach for $EEMT_{TOPO}$ was designed to explicitly incorporate topographic variations in solar radiation, temperature, wind speed, and vapor pressure deficit. Specifically, PET was calculated using a Penman–Montieth approach to estimate pan evaporation (see Supplemental Material) that was then coupled with an estimation of the AET using a Budyko curve (Budyko, 1974) describing the partitioning of potential and actual evapotranspiration relative to the aridity index (ratio of annual PET to annual rainfall). Potential evapotranspiration and precipitation were converted to monthly values of AET (m s^{-1}) using a Zhang–Budyko curve that describes the climatological relationship between the relative partitioning of catchment-scale precipitation to PET and AET as (Zhang et al., 2001)

$$AET_{ZB} = PPT\left\{1 + \frac{PET_{pm}}{PPT} - \left[1 + \left(\frac{PET_{pm}}{PPT}\right)^{w}\right]^{1/w}\right\} \qquad [8]$$

where w is an empirical constant, here set equal to 2.63 following Zhang et al. (2004). This catchment-scale approach to precipitation partitioning was then scaled to local topography based on incorporation of topographic redistribution of effective precipitation (below). It is likely that w varies with the local climate, vegetation, and subsurface storage regimes that span the study watershed, e.g., Zhang et al. (2004) determined optimum w values ranging from 2.15 to 3.75 for temperate forest and grassland systems, respectively. However, for simplicity and the lack of a clear empirical means to assign a w value to specific ecosystems, we applied a constant value of w to all ecosystems.

Evapotranspiration for Topographic and Vegetation Modified Effective Energy and Mass Transfer

The approach to calculating $EEMT_{TOPO\text{-}VEG}$ used the Penman–Montieth equation that includes the surface resistance term in the denominator and a canopy-derived estimate of aerodynamic resistance to provide an estimate of the actual evapotranspiration (AET_{pm}) (see Supplemental Material). The aerodynamic resistance term was calculated using the canopy height derived from the LiDAR data, and surface resistance was estimated from the LAI. Following data reported by Schulze et al. (1994) and Kelliher et al. (1995), we fit a polynomial function relating bulk surface conductance to LAI assuming a maximum leaf stomatal conductance of 0.008 m s^{-1}. This approach does not account for species- and ecosystem-level differences in stomatal conductance. The ecosystems included in the study area range from desert scrub to mixed conifer forests. Previous research has indicated that the maximum stomatal conductance measured in various conifer species to sclerophyllous shrubs ranges from 0.0038 to 0.0082 m s^{-1}, comparable to the 0.008 m s^{-1} value used here (Kelliher et al., 1995). Surface resistance was taken as the inverse of the bulk surface conductance, with values ranging from 38 to 55 s m^{-1}. For any months of AET_{pm} > PPT, we assumed that AET was equivalent to PPT and P_{eff} was set equal to zero.

Topographic Water Redistribution

The wetting of each pixel is a function of both effective precipitation and surface runoff as noted in the rearrangement of Eq. [7] to $F = P_{eff} - SR$. It is thus necessary to account for topographic redistribution and partitioning of precipitation to quick surface runoff in addition to local-scale variation in P_{eff}. One standard approach to empirically quantifying topographic control on water redistribution is the topographic wetness index, calculated as (Beven and Kirkby, 1979) $\lambda = \ln(a/\tan\beta)$, where a is the unit or specific catchment area in meters, calculated here using the D-inf multiple-flow-direction algorithm for flow routing (Tarboton et al., 1991), and β is the slope in degrees. The wetness index provides empirical measures of relative landscape wetness but does not provide a mass-conservative approach to redistributing effective precipitation across a catchment.

We developed a modified topographic wetness index, referred to as the *mass conservative wetness index* (MCWI) and denoted with the symbol α, which accounts for topographic redistribution of effective precipitation and maintains conservation of mass of catchment-scale precipitation inputs. We argue that a_i is proportional to the local pixel wetness index (l_i) normalized to the mean catchment wetness index ($\bar{\lambda}$):

$$\alpha_i \propto \frac{\lambda_i}{\bar{\lambda}} \qquad [9]$$

such that $\alpha_i = \lambda_i/(1/N)\Sigma\lambda_i$ and $\Sigma\alpha_i = N$, where N is the number of pixels in a catchment. The normalization ensures conservation of mass of the effective precipitation term for a given catchment. The scalability of a_i was tested by comparing estimations of a_i using $\bar{\lambda}$ calculated for both local subcatchments and for the entire study area (Supplemental Fig. S2); the 1:1 scaling between the two values indicates that there is not a catchment-size effect on a_i.

Calculated MCWI values ranged from 0.4 to 3.4, with the lowest values on divergent hillslope summits and ridgelines and the greatest values in drainageways, particularly the low-elevation drainageways that have large catchment areas (Fig. 3c). These values indicate that local effective precipitation may be reduced by up to 60% due to runoff, whereas drainageways may receive water (as soil moisture) in excess of up to 340% over local effective precipitation inputs.

The fraction of monthly P_{eff} partitioned to F at each pixel (F_i, m s^{-1}) using this modified topographic wetness index was determined as

$$F_i = \alpha_i P_{eff\,i} \qquad [10]$$

Primary Production and Standing Biomass

Net primary production was calculated differently for each EEMT modeling approach, reflecting incorporation of increasing levels of topographic and vegetative information. The NPP calculation for $EEMT_{TRAD}$ was based on the temperature of the months in which precipitation is greater than evapotranspiration. For these months, NPP was calculated following Lieth (1975): $NPP = 3000[1 - \exp(1.315 - 0.119T)]^{-1}$. Using this equation, NPP was calculated on a monthly time step for all months of PPT > PET, and NPP was scaled to a monthly time step based on each month's percentage of 1 yr. This method of NPP estimation does not account for primary production that occurs using stored soil moisture and thus probably underestimates total NPP. However, comparison of NPP calculated using this method relative to global NPP data sets indicates reasonable agreement between the two (Rasmussen and Gallo, 2013; Rasmussen et al., 2005).

For the $EEMT_{TOPO}$ approach, we incorporated information on elevation and aspect using an empirical function fit to NPP data presented by Whittaker and Niering (1975) for the SCM. Aspect and slope were converted to the unitless parameter "northness," which is the product of the cosine of aspect and the sine of slope and ranges from −1 for a south-facing, vertical cliff to 1 for a north-facing vertical cliff (Fig. 3d). Total annual aboveground NPP (g m^{-2} yr^{-1}) was regressed against elevation and northness with the best-fit multiple linear regression model of

$$NPP = 0.39z + 346n - 187 \qquad [11]$$

where z is elevation in meters and n is northness, with $r^2 = 0.82$, $P < 0.0001$, and RMSE = 168 g m^{-2} yr^{-1}. Any predicted values <100 g m^{-2} yr^{-1} were adjusted to 100 g m^{-2} yr^{-1} to match the minimum NPP measurements in the Whittaker and Niering (1975) data set.

For the $EEMT_{TOPO\text{-}VEG}$ approach, annual NPP (g m^{-2} yr^{-1}) was calculated as a function of canopy height, derived from the LiDAR data, using a polynomial function relating canopy height and aboveground NPP using data reported by Whittaker and Niering (1975):

$$\mathrm{NPP} = 196 + 36h - (0.61h - 12.0933) \quad [12]$$

where h is canopy height (m) derived from the LiDAR data, with $r^2 = 0.89$, $P < 0.0001$, and RMSE = 130 g m^{-2} yr^{-1}.

Standing biomass (Mg ha^{-1}) was calculated from the LiDAR mean canopy height (mch) profile (Asner et al., 2011; Lefsky et al., 1999; Mascaro et al., 2011). The model parameters were determined from a regression of the field-measured biomass from 13 0.1-ha plots in the SCM (1.3 ha), 79 0.05-ha plots in the Pinaleño Mountains, Arizona (3.65 ha), and 48 0.1-ha plots in the Jemez River Basin, New Mexico (4.8 ha) (Swetnam, 2013):

$$\mathrm{Biomass} = 1.441\ \mathrm{mch}^{2.151} \quad [13]$$

All three study areas shared the same plant functional type groups (Smith et al., 1997), where the presence and frequency of species in the stand are all closely related. Average biomass measured in the SCM plots was 226.66 ± 125.84 Mg ha^{-1}; the peak quantity of biomass measured in any plot in the three study areas was in the Pinaleño Mountains, where an equivalent of 1495 Mg ha^{-1} was measured in the 0.05-ha plots. Similar stand conditions and life histories are shared between the Pinaleño Mountains and the SCM (Niering and Lowe, 1984; Whittaker and Niering, 1975). In a similar plot in the SCM (white fir [*Abies concolor* (Gordon & Glend.) Lindl. ex Hildebr.] ravine forest), Whittaker and Niering reported 790 Mg ha^{-1} of aboveground biomass.

Effective Energy and Mass Transfer

The individual components of EEMT were calculated as in Eq. [4] and [5] and the EEMT term calculated as in Eq. [3] for each pixel on a monthly basis. To summarize, the three approaches to calculating EEMT varied in the derivation of the F and NPP terms and incorporated greater levels of environmental information. Specifically: (i) $\mathrm{EEMT_{TRAD}}$ was based on F derived from the balance of precipitation and PET and NPP derived using the Lieth empirical function; (ii) $\mathrm{EEMT_{TOPO}}$ was calculated based on F derived using the coupled Penman–Budyko approach to calculating AET and the MCWI to account for local variations in water redistribution, and NPP was calculated from the empirical relationship between NPP, northness, and elevation; and (iii) $\mathrm{EEMT_{TOPO\text{-}VEG}}$ was calculated using F derived from the balance of precipitation and AET calculated using Penman–Monteith that accounted for local surface resistance and canopy-influenced aerodynamic resistance, the MCWI to account for local variations in water redistribution, and NPP derived from the empirical relationship between LiDAR-measured canopy height and NPP. The correlation among environmental variables and the various EEMT values are presented in Supplemental Table S1, with an analysis of factor importance to EEMT prediction for each method determined using a simple multiple linear regression approach (Supplemental Table S2).

Results and Discussion

Watershed Climate Classification

Climate forcing parameters of temperature and precipitation vary consistently and inversely with elevation across the study area, i.e., decreasing temperature and increasing precipitation with increasing elevation, as is typical of mountainous ecosystems in the Desert Southwest (DeBano et al., 1995) (Fig. 3a and 3b). Climate across the watershed was characterized using an aridity index derived from modeled climate parameters to account for this covariance and to facilitate a simpler discussion of EEMT variation with climate and elevation. Values for the aridity index, defined as the ratio between $\mathrm{PET_H}$ and MAP, ranged from a maximum of 2.5 in the low-elevation systems to a minimum of 0.6 in the high-elevation systems. The $\mathrm{PET_H}$/MAP data were classified into five classes using a hierarchical classification scheme based on Ward's minimum variance method to define the distance between classes (Milligan, 1979). The number of classes was determined by iterating with various numbers of classes, ranging from 3 to 10. It was determined that five was the fewest number of classes required to best capture the transition in climate from water-limited ($\mathrm{PET_H}$/MAP > 1) to energy-limited ($\mathrm{PET_H}$/MAP < 1) systems. The classification scheme was specifically focused to capture the transition from energy- to water-limited systems because this represents a key transition in hydrologic function and vegetation composition (Brooks et al., 2011). The five classes were categorized and named based on $\mathrm{PET_H}$/MAP ranges into the following (Table 1):

Table 1. Aridity class potential evapotranspiration/mean annual precipitation (PET/MAP) values and associated elevation, vegetation, and effective energy and mass transfer using the traditional method ($\mathrm{EEMT_{TRAD}}$), EEMT with topographic controls ($\mathrm{EEMT_{TOPO}}$), and EEMT with both topographic and vegetation controls ($\mathrm{EEMT_{TOPO\text{-}VEG}}$).

Aridity index class	PET/MAP	Elevation	Canopy height	Biomass	$\mathrm{EEMT_{TRAD}}$	$\mathrm{EEMT_{TOPO}}$	$\mathrm{EEMT_{TOPO\text{-}VEG}}$
		m	m	Mg ha^{-1}	——MJ m^{-2} yr^{-1}——		
Humid	0.70 ± 0.05†	2433 ± 113	5.44 ± 4.57	104.9 ± 190.7	33.7 ± 2.9	23.1 ± 3.4	21.2 ± 11
Humid transition	0.89 ± 0.07	2080 ± 115	2.34 ± 2.19	19.4 ± 56.4	24.4 ± 3.2	19.1 ± 3.5	12.1 ± 5.8
Arid transition	1.18 ± 0.09	1683 ± 101	1.19 ± 1.18	4.9 ± 17.3	14.1 ± 2.4	15.0 ± 3.8	9.0 ± 3.1
Semiarid	1.51 ± 0.1	1365 ± 84	0.78 ± 1.03	2.9 ± 20.6	7.6 ± 1.0	11.4 ± 3.4	7.6 ± 2.1
Arid	1.97 ± 0.2	1063 ± 107	0.77 ± 0.76	1.9 ± 9.9	5.5 ± 0.5	8.0 ± 3.1	6.7 ± 1.4

† Mean ± 1σ.

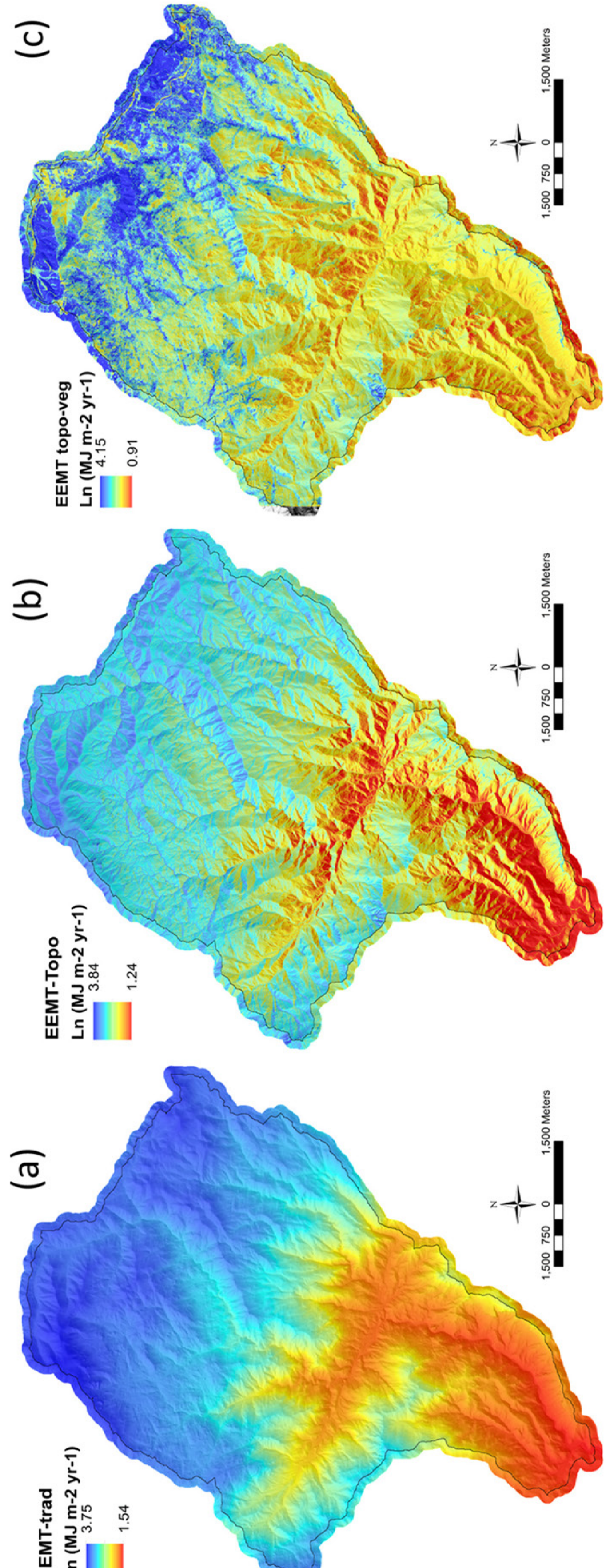

Fig. 4. Values for effective energy and mass transfer calculated for the Sabino Creek watershed using the (a) "traditional" method that does not include local topographic variation or vegetation (EEMT-trad), the (b) topographic method that includes topographic control on wetness, solar radiation, and primary productivity (EEMT-Topo), and (c) the topographic and vegetation method that incorporates LiDAR-derived vegetation and National Agriculture Imagery Program derived leaf area index to parameterize the full Penman–Monteith approach to calculating actual evapotranspiration (EEMT topo-veg). All values are natural logarithm transformed to optimize presentation of the data.

1. *Humid* with a range of 0.6 to 0.8
2. *Humid transition* with a range of 0.8 to 1.0
3. *Arid transition* with a range of 1.0 to 1.3
4. *Semiarid* with a range of 1.3 to 1.7
5. *Arid* with a range of 1.7 to 2.5

The classes correspond with an approximate 300-m elevation gain interval and with changes in vegetation community (Table 1), grading from humid classes at high elevation dominated by coniferous ecosystems, to transitional classes at mid-elevation that include the transition from open grass oak woodland to mixed oak and pine forest plant communities, to arid classes at low elevation occupied by desert scrub. Canopy height and biomass increased with elevation and wetness (Table 1). Vegetation assemblage and LAI followed the variation in elevation-controlled climate parameters and local topographic controls on MCWI and northness (Fig. 3).

Measures of Effective Energy and Mass Transfer

Traditional Effective Energy and Mass Transfer

Values for $\text{EEMT}_{\text{TRAD}}$ ranged from a low near 5 MJ m^{-2} yr^{-1} in low-elevation, very dry desert scrub systems to a maximum of just over 42 MJ m^{-2} yr^{-1} in the wet, mixed conifer, high-elevation systems (Fig. 4a). The values varied directly with elevation following the elevation control on climatological parameters. This range of values corresponds well with $\text{EEMT}_{\text{TRAD}}$ ranges calculated previously using the 4-km and 800-m pixel resolution PRISM climate data set (Rasmussen et al., 2005) that ranged from 10 to 35 MJ m^{-2} yr^{-1}, and with an initial attempt to incorporate topography into EEMT estimates at a 10-m pixel resolution using an empirical relationship derived among EEMT, temperature, precipitation, and vapor pressure deficit (Chorover et al., 2011) that ranged from <5 to 37 MJ m^{-2} yr^{-1}.

Effective Energy and Mass Transfer with Topographic Control

Values for $\text{EEMT}_{\text{TOPO}}$ ranged from a minimum of 3.5 MJ m^{-2} yr^{-1} at low elevation up to a maximum of 46.5 MJ m^{-2} yr^{-1} at high elevation (Fig. 4b). As with $\text{EEMT}_{\text{TRAD}}$, the values for $\text{EEMT}_{\text{TOPO}}$ increased with elevation and increasing water availability but also exhibited distinct variation with aspect and local wetness within each aridity index class (Table 2). Values for $EEMT_{TOPO}$ were generally on the order of 5 MJ m^{-2} yr^{-1} greater on north-facing slopes than south-facing slopes, with the largest difference of 5.7 MJ m^{-2} yr^{-1} noted in the arid transition class and the smallest difference of 4.6 MJ m^{-2} yr^{-1} observed in the arid class. Similarly, $EEMT_{TOPO}$ values tended to be greater in water-gaining portions of the landscape, with values on average 1.4 MJ m^{-2} yr^{-1} greater in areas with MCWI values >1. The largest $EEMT_{TOPO}$ difference of 1.9 MJ m^{-2} yr^{-1} was observed in the humid transition class, with the smallest difference 0.6 MJ m^{-2} yr^{-1} observed in the arid class.

Aspect and topographic wetness had varying impacts on $EEMT_{TOPO}$, with some variation among aridity classes (Table 2). Generally greater values of $EEMT_{TOPO}$ were predicted on north-facing slopes, with values averaging 5 MJ m^{-2} yr^{-1} greater on slopes with northness values >0 (Table 2). The smallest aspect difference of 4.6 MJ m^{-2} yr^{-1} was observed in the arid class, where differences were probably minimized due to the overall aridity of this portion of the SCM. In comparison, the largest aspect difference of 5.7 MJ m^{-2} yr^{-1} was observed in the arid transition class on the boundary of water and energy limitation, where aspect-controlled variation in radiative forcing and temperature produced greater differences in water availability and primary production. The values for $EEMT_{TOPO}$ for north-facing slopes in a given aridity class generally corresponded closely to the mean $EEMT_{TOPO}$ values for south-facing slopes in the next wetter class, e.g., an average $EEMT_{TOPO}$ value of 22.5 MJ m^{-2} yr^{-1} on the north-facing slopes in the humid transition class relative to an average of 21.2 MJ m^{-2} yr^{-1} on the south-facing slopes in the humid class. This pattern was consistent across all aridity classes, indicating that north-facing slopes in a given climate zone function similarly to wetter ecosystems, equivalent to an approximate 300-m elevation gain (Table 1). A similar pattern has been observed in vegetation patterning and soil properties across the SCM (Lybrand and Rasmussen, 2014; Pelletier et al., 2013; Whittaker et al., 1968) and other elevation gradients in the western United States (Poulos et al., 2010).

Variation in $EEMT_{TOPO}$ between water-gaining (MCWI > 1) and water-losing (MCWI < 1) landscape positions were less pronounced than those associated with aspect, with an average increase of 1.4 MJ m^{-2} yr^{-1} in water-gaining portions of the landscape. The difference between losing and gaining positions increased with moisture availability and aridity index class (Table 2), probably a function of greater water available to redistribute to gaining portions of the landscape. The MCWI as applied here does not account for runoff response to rainfall characteristics, e.g., high-intensity monsoon rainfall that may exceed surface soil infiltration rates with the potential for substantial water redistribution from losing to gaining portions of the landscape even in the semiarid and arid systems (Zhang et al., 2011).

Effective Energy and Mass Transfer with Topographic and Vegetation Control

The values for $EEMT_{TOPO\text{-}VEG}$ ranged from 2.5 to 63.4 MJ m^{-2} yr^{-1}, increasing from low to high elevation similar to the other values for EEMT (Fig. 4c). The highest values of EEMT, 35 to 63 MJ m^{-2} yr^{-1}, were spatially constrained to those areas with an elevation greater than ~2000 m asl and PET_H/MAP < 1.0, corresponding to predominantly pine and mixed conifer ecosystems. Differences in EEMT with aspect and topographic wetness averaged 3.9 and 0.9 MJ m^{-2} yr^{-1}, respectively, but exhibited substantial variation with aridity index class (Table 3). The EEMT differences by aspect increased with increasing water availability, with a large increase in the relative differences observed in the humid class. Similar to values predicted for $EEMT_{TOPO}$, average north-aspect $EEMT_{TOPO\text{-}VEG}$ values for a given aridity class were comparable to average $EEMT_{TOPO\text{-}VEG}$ values for south-facing slopes in

Table 2. Mean effective energy and mass transfer with topographic controls ($EEMT_{TOPO}$) by aspect and wetness index grouped by aridity index class.

	Aspect			Wetness index		
Aridity index class	North	South	Difference	Gaining	Losing	Difference
Humid	26.2 ± 2.71†	21.16 ± 2.19	5.04 ± 0.01	24.03 ± 3.35	22.49 ± 3.34	1.54 ± 0.014
Humid transition	22.45 ± 2.57	17.43 ± 2.56	5.02 ± 0.01	22.45 ± 2.57	17.43 ± 2.56	1.91 ± 0.013
Arid transition	18.65 ± 2.87	12.98 ± 2.45	5.67 ± 0.013	20.39 ± 3.5	18.48 ± 3.29	1.55 ± 0.019
Semiarid	14.37 ± 2.25	9.24 ± 2.3	5.13 ± 0.011	18.65 ± 2.87	12.98 ± 2.45	1.3 ± 0.017
Arid	10.72 ± 2.35	6.11 ± 1.81	4.61 ± 0.012	16.04 ± 3.67	14.49 ± 3.71	0.64 ± 0.018
Mean			5.08 ± 0.34			1.39 ± 0.42

† Mean ± 1σ.

Table 3. Mean effective energy and mass transfer with topographic and vegetation controls ($EEMT_{TOPO\text{-}VEG}$) by aspect and wetness index grouped by aridity index class.

	Aspect			Wetness index		
Aridity index class	North	South	Difference	Gaining	Losing	Difference
Humid	26.69 ± 11.11†	18.07 ± 9.14	8.62 ± 0.04	22.89 ± 11.55	20.39 ± 10.13	2.49 ± 0.043
Humid transition	15.01 ± 6.41	10.78 ± 4.84	4.22 ± 0.021	12.99 ± 6.47	11.78 ± 5.34	1.22 ± 0.022
Arid transition	10.94 ± 2.19	7.92 ± 2.48	3.02 ± 0.014	9.11 ± 2.98	8.96 ± 3.19	0.15 ± 0.016
Semiarid	8.81 ± 1.56	6.67 ± 1.92	2.13 ± 0.009	7.78 ± 1.92	7.49 ± 2.13	0.28 ± 0.01
Arid	7.43 ± 1.05	6.09 ± 1.34	1.34 ± 0.007	6.89 ± 1.36	6.51 ± 1.39	0.38 ± 0.008
Mean			3.87 ± 2.56			0.90 ± 0.88

† Mean ± 1σ.

the next wetter humidity class. Differences in $EEMT_{TOPO-VEG}$ between water-gaining and water-losing landscapes increased with increasing water availability, but overall exhibited minimal variation. In general, the largest impacts of topography and vegetation on $EEMT_{TOPO-VEG}$ values were observed in the energy-limited humid ecosystems that are dominated by mixed conifer vegetation assemblages and are the most biologically productive (Whittaker and Niering, 1975). These systems also exhibit the greatest soil C stocks, degree of chemical weathering, and soil development (Lybrand and Rasmussen, 2014).

Vegetation Effects on Effective Energy and Mass Transfer

The effects of vegetation on the calculated EEMT was evident in the spatial patterning exhibited in $EEMT_{TOPO-VEG}$ (Fig. 4c). This result was expected because vegetation is incorporated into energy, water, and C balances through the LAI constraint on surface temperature estimates (Eq. [6]), the surface resistance term in AET estimates (Eq. [12]), and the modeled relation of canopy height to NPP (Eq. [16]). Multiple linear regression analysis of $EEMT_{TOPO-VEG}$ relative to elevation, northness, MWCI, and canopy height indicated that canopy height was the most important factor accounting for variations in $EEMT_{TOPO-VEG}$ (Supplemental Table S2). In particular, predictions of AET using Penman–Monteith are highly sensitive to surface resistance (Shuttleworth, 1993). The predicted surface resistance estimates were reasonable and in the range of 38 to 55 s m^{-1} but probably introduce the largest source of error and spatial variation into the water balance used to calculate $EEMT_{TOPO-VEG}$.

We further examined the relative impact of vegetation incorporation into EEMT estimates through comparison of the ratio between $EEMT_{TOPO-VEG}$ and $EEMT_{TOPO}$ by aridity class (Fig. 5a). The data were a subset of data for those locations with no or low burn severity to avoid any confounding effects of fire. Values for $EEMT_{TOPO-VEG}/EEMT_{TOPO}$ indicated minimal differences in EEMT estimates for the arid and humid classes, with mean ratios of 1.08 and 0.91, respectively. The largest differences between the two methods for calculating EEMT were observed for the humid transition and arid transition classes, with average ratio values of 0.62, indicating that $EEMT_{TOPO}$ values were greater than $EEMT_{TOPO-VEG}$ values. The differences between the two EEMT values are a direct function of vegetation in that $EEMT_{TOPO-VEG}$ incorporates the current vegetation structure into its estimates of water and C fluxes. We suggest that $EEMT_{TOPO}$ provides a maximum "potential" estimate of EEMT, whereas $EEMT_{TOPO-VEG}$ reflects current or "actual" energy and mass transfers based on the current vegetation structure.

The greatest difference between the two estimates was observed at the water- to energy-limited transition zone. This zone probably represents the zone of greatest dynamism in vegetation structure and composition because it bounds the transition zone in the water balance and is associated with the transition from mainly grass, shrub, and open woodland plant communities to more mixed pine and oak forest (Whittaker and Niering, 1975). The current vegetation structure in this zone is probably a function of both longer term, e.g., centennial time scales, and shorter term, e.g., annual to decadal, fluctuations in climate-controlled water availability and drought. Climate fluctuation is also coupled with the time scales of the vegetation response to changes in climate that vary with vegetation type, e.g., long-lived trees may not reflect recent changes in water availability that would favor more temporally dynamic grasses and shrubs (Walther et al., 2002).

The spatial patterns of $EEMT_{TOPO-VEG}$, particularly at high elevations (Fig. 4c), indicated a negative trend to increasing burn severity class from the 2003 Aspen fire that occurred approximately 7 yr before acquisition of the NAIP image and LiDAR collection. The differences in $EEMT_{TOPO-VEG}$ and $EEMT_{TOPO}$

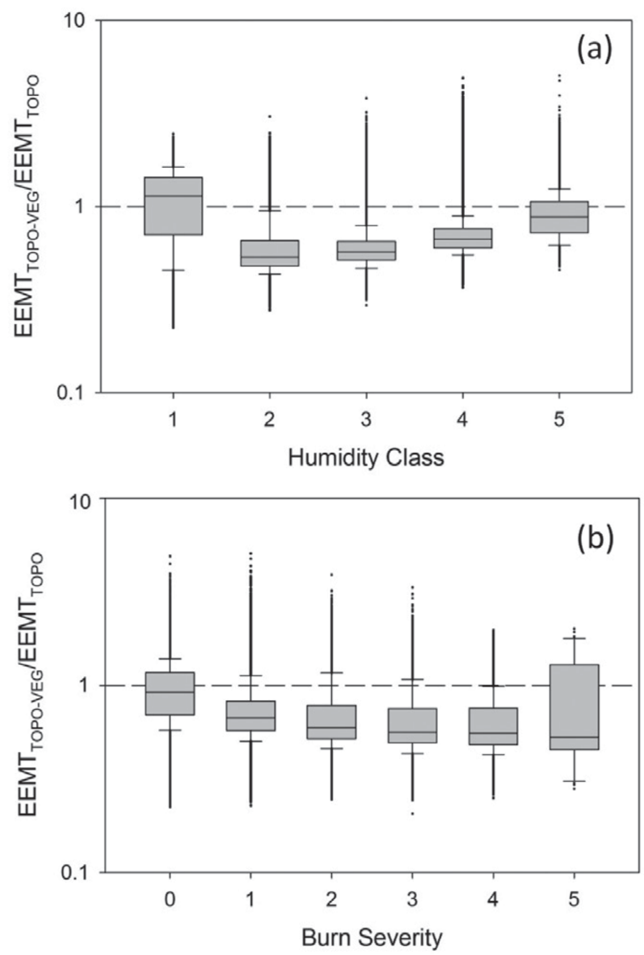

Fig. 5. Comparison of the natural logarithm of the ratio between effective energy and mass transfer with topographic controls ($EEMT_{TOPO}$) and effective energy and mass transfer with topographic and vegetation controls ($EEMT_{TOPO-VEG}$) by (a) aridity/humidity class and (b) burn severity. Ratio values of 1 indicate identical values for the two measures of EEMT, denoted by a dashed line in both figures. Deviation from the 1 line indicates divergence between the two measures of EEMT.

increased significantly with increasing burn severity, with ratio values decreasing from a mean of 0.95 for areas that did not burn, to a mean of 0.64 for the high-severity burn areas (Fig. 5b). Lower ratios suggest a greater differential between maximum potential EEMT and actual EEMT recorded in the current vegetation structure. Disturbance events, such as wildfire, that remove vegetation and alter local patterns of evaporation and primary production thus serve to reduce the modeled values of $EEMT_{TOPO\text{-}VEG}$ relative to the idealized conditions modeled with $EEMT_{TOPO}$.

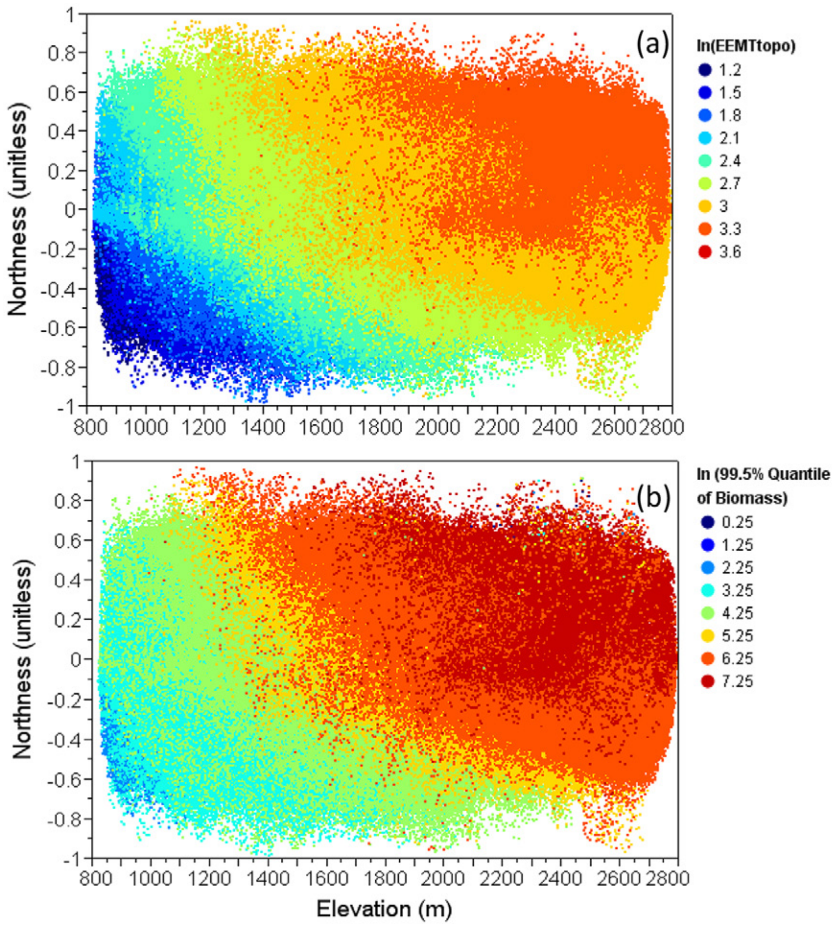

Fig. 6. Variation in (a) effective energy and mass transfer with topographic controls ($EEMT_{TOPO}$) and (b) the upper 99.5% quantile of biomass by topographic northness (a combination of aspect and slope) and elevation. The data indicate that both values increase with elevation and northness in a similar pattern.

Biomass Relationship to Effective Energy and Mass Transfer

The average 10-m pixel mean canopy height across the Sabino Creek watershed ranged from 0 to 26 m, with the biomass estimated to range from 19 to 1600 Mg ha^{-1} based on the 99.5% quantile of canopy height and biomass values. The 99.5% quantiles were used to exclude very high values of canopy height that yield unreasonably high biomass values. The 99.5% quantile values were similar to independent measures of aboveground biomass in the SCM (Whittaker and Niering, 1975) and Pinaleño Mountains nearby in southeastern Arizona (Pelletier et al., 2013; Swetnam, 2013) that reported maximum measurements on the order of 790 to 1500 Mg ha^{-1}, respectively.

Both $EEMT_{TOPO}$ and biomass exhibited similar patterns of increase with both elevation and northness (Fig. 6), suggesting that $EEMT_{TOPO}$ may be used to predict the maximum biomass for a given area. Direct comparison of biomass to $EEMT_{TOPO}$ indicated a power law relationship in the form of Biomass = $m EEMT_{TOPO}{}^{b}$. The power function was fit to the 99.5% quantile of biomass and $EEMT_{TOPO}$, yielding parameters of $m = 0.032 \pm 0.0075$ kg m^{2} yr ha^{-1} MJ^{-1} and $b = 3.22 \pm 0.071$, with an equation fit of $r^2 = 0.98$, $P < 0.0001$, and RMSE of 69.7 Mg ha^{-1} (Fig. 7). The model fit well the overall trend in the data, with the largest discrepancy between actual and predicted values noted near the inflection point of the function at $EEMT_{TOPO}$ values of ~12 to 18 MJ m^{-2} yr^{-1}. This zone corresponds with the dry and wet transition humidity classes and suggests a possible break in scaling between biomass and $EEMT_{TOPO}$. At high values of $EEMT_{TOPO}$, biomass tended to decrease. These areas correspond to those impacted by moderate and severe burns and a loss of standing biomass. The power law relationship suggests that $EEMT_{TOPO}$ may provide an upper bound estimate for standing biomass for what the potential for aboveground biomass could attain in these areas. The relationship of biomass to $EEMT_{TOPO}$ probably reaches a plateau beyond $EEMT_{TOPO}$ values of 35 to 40 MJ m^{-2} yr^{-1}, as suggested by global upper limits on aboveground biomass in temperate conifer forests on the order of 1600 to 1800 Mg ha^{-1} (Keith et al., 2009).

Comparison of Effective Energy and Mass Transfer Values to Soil Depth

The separate sets of EEMT values were directly compared with measured and modeled values of soil depth for a small ~5-ha forested catchment in the headwaters of Sabino Creek as a means to document the relative improvement that incorporation of topography and vegetation into EEMT imparts on predicting pedon- to hillslope-scale CZ structural variation. The soil depth data derive from previous work in the SCM and represent the most robust set of soil depth data we have collected to date (Holleran et al., 2014; Pelletier and Rasmussen, 2009). The catchment is at a mean elevation of 2400 m asl, with mixed conifer vegetation, granitic parent material, and soils that include a combination of Entisols on ridges and slopes and Mollisols in convergent water-gathering portions of the landscape (Holleran, 2013; Lybrand and Rasmussen, 2014). The soil depth data included 24 pedons and soil depth derived from a numerical model describing soil production and mass transport.

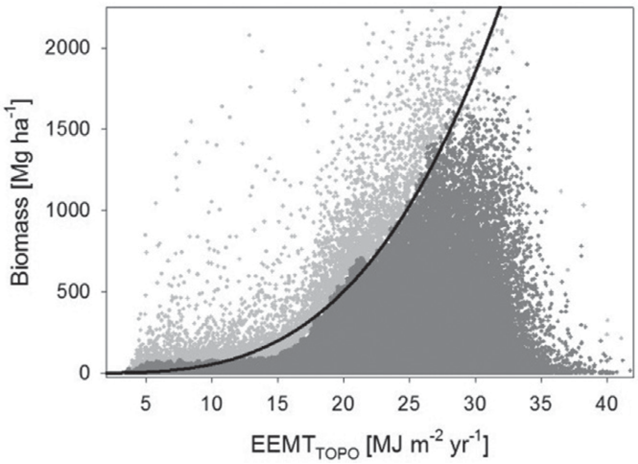

Fig. 7. Relationship between effective energy and mass transfer with topographic controls (EEMT$_{TOPO}$) and biomass. Dark gray symbols are those points within the 99.5% quantile; light gray points are greater than the 99.5% quantile. The black line is the best-fit power law function in the form of: Biomass = mEEMT$_{TOPO}{}^{b}$, where m is 0.032 and b is 3.22 with an RMSE of 69.7 Mg ha^{-1}.

Measured and modeled soil depths range from ~0.15 m on ridgetops to >2 m in convergent areas of the landscape. Values for EEMT$_{TRAD}$, EEMT$_{TOPO}$, and EEMT$_{TOPO\text{-}VEG}$ were extracted for each pedon location and modeled soil depth pixel. Simple correlation analyses revealed significant variation in the relationships among the sets of EEMT values and the soil depth data (Table 4). The vales for EEMT$_{TOPO}$ exhibited the strongest and most significant positive correlations to both measured and modeled soil depth data, indicating that incorporation of topographic controls on local energy and water balance and primary productivity significantly increased the positive relationship between EEMT and pedon- to hillslope-scale measures of CZ structural variability.

The relative lack of correlation between soil depth and EEMT$_{TOPO\text{-}VEG}$ suggests that, for this location, the current vegetation stand has minimal influence on soil depth. The variance in EEMT$_{TOPO\text{-}VEG}$ is largely attributed to canopy height data (Supplemental Table S2) that represent only one snapshot in time. We suggest that EEMT$_{TOPO}$ presents a stronger relationship than EEMT$_{TOPO\text{-}VEG}$ because it better captures spatial patterns in the long-term average, i.e., >10^3 yr, fluxes of water and C into the subsurface,

Table 4. Pairwise correlation of soil depth data and effective energy and mass transfer using the traditional method (EEMT$_{TRAD}$), EEMT with topographic controls (EEMT$_{TOPO}$), and EEMT with both topographic and vegetation controls (EEMT$_{TOPO\text{-}VEG}$) for a small catchment in the headwaters of Sabino Creek. The data include point-measured (pit) soil depth data and numerically modeled soil depth data for the selected catchment.

	Pit data (n = 24)		Model data (n = 319)	
EEMT method	r	P value	r	P value
EEMT$_{TRAD}$	−0.038	0.861	−0.058	0.298
EEMT$_{TOPO}$	0.385	0.063	0.569	<0.0001
EEMT$_{TOPO\text{-}VEG}$	−0.019	0.929	0.131	0.019

whereas EEMT$_{TOPO\text{-}VEG}$ captures only the modern signature that may not reflect longer time scale patterns. This was clearly demonstrated in the large discrepancy between EEMT$_{TOPO}$ and EEMT$_{TOPO\text{-}VEG}$ for areas that recently experienced severe wildfire. Estimations of EEMT$_{TOPO\text{-}VEG}$ may be improved by incorporating decadal scale time series of canopy height and LAI that better describe longer term patterns of vegetation structure and localized primary production. The data suggest that EEMT$_{TOPO}$ presents the more robust predictor of CZ structure, function, and evolution over the long term and represents a measure of the potential or optimum influx of energy and mass to the CZ.

Summary

The analyses in this study indicated clear patterns in the EEMT to the subsurface CZ with topography and vegetation. Incorporating greater levels of environmental information introduced greater local complexity in EEMT, with clear variation in EEMT by aspect and with current vegetative cover. Key findings include:

- Greater values of EEMT were observed on north-facing slopes within a given aridity class and elevation zone, equivalent to a 300-m elevation gain. This pattern corresponds with observed aspect variation in modern canopy height and indicates clear aspect control on energy and mass influxes to the CZ that are probably important to understanding aspect-controlled variation in CZ evolution, structure, and function.

- The largest discrepancies in EEMT$_{TOPO}$ and EEMT$_{TOPO\text{-}VEG}$ were observed at the water- to energy-limited system transition where current vegetation structure is highly sensitive to local variations in the water and energy balances. Disturbance in the form of stand-replacing wildfire also substantially reduced estimates of EEMT$_{TOPO\text{-}VEG}$ relative to EEMT$_{TOPO}$ as a result of a reduction in biomass, primary productivity, and variations in surface and aerodynamic resistance. The discrepancy between the two EEMT values indicates deviation between what could be considered the long-term average energy and mass influx, or EEMT$_{TOPO}$, and the current vegetation stand controlled energy and mass influx, or EEMT$_{TOPO\text{-}VEG}$.

- A power law relationship was observed between aboveground biomass and EEMT$_{TOPO}$, indicating the potential for using EEMT$_{TOPO}$ to predict an upper bound for biomass in a given area.

- The incorporation of topography and vegetation significantly increased the correlative relationship between EEMT and subsurface CZ structure as quantified here as soil depth. In particular, EEMT$_{TOPO}$ exhibited the strongest positive correlation to measured and modeled values of soil depth, indicating that this version of EEMT may serve as an effective predictor of CZ properties that captures pedon- to hillslope-scale variation in water and C influxes.

Acknowledgments

This research was supported by the U.S. National Science Foundation Grants EAR-0724958630 and EAR-1331408 provided in support of the Catalina-Jemez Critical Zone Observatory.

References

Arkley, R.J. 1963. Calculation of carbonate and water movement in soil from climate data. Soil Sci. 96:239–248. doi:10.1097/00010694-196310000-00003

Asner, G.P., R.F. Hughes, J. Mascaro, A.L. Uowolo, D.E. Knapp, J. Jacobson, et al. 2011. High-resolution carbon mapping on the million-hectare Island of Hawaii. Front. Ecol. Environ 9:434–439. doi:10.1890/100179

Beaudette, D.E., and A.T. O'Geen. 2009. Quantifying the aspect effect: An application of solar radiation modeling for soil survey. Soil Sci. Soc. Am. J. 73:1345–1352. doi:10.2136/sssaj2008.0229

Beven, K.J., and M.J. Kirkby. 1979. A physically based, variable contributing area model of basin hydrology. Hydrol. Sci. Bull. 24:43–69. doi:10.1080/02626667909491834

Brooks, P.D., P.A. Troch, M. Durcik, E. Gallo, and M. Schlegel. 2011. Quantifying regional scale ecosystem response to changes in precipitation: Not all rain is created equal. Water Resour. Res. 47:W00J08. doi:10.1029/2010WR009762

Broxton, P.D., P.A. Troch, and S.W. Lyon. 2009. On the role of aspect to quantify water transit times in small mountainous catchments. Water Resour. Res. 45:W08427. doi:10.1029/2008WR007438

Budyko, M.I. 1974. Climate and life. Academic Press, San Diego.

Chorover, J., R. Kretzschmar, and D.L. Sparks. 2007. Soil biogeochemical processes withing the critical zone. Elements 3:321–326.

Chorover, J., P.A. Troch, C. Rasmussen, P.D. Brooks, J.D. Pelletier, D.D. Breshears, et al. 2011. How water, carbon, and energy drive critical zone evolution: The Jemez-Santa Catalina Critical Zone Observatory. Vadose Zone J. 10:884–899. doi:10.2136/vzj2010.0132

DeBano, L.F., P.H. Ffolliott, A. Ortega-Rubio, G.J. Gottfried, R.H. Hamre, and C.B. Edminster, technical coordinators. 1995. Biodiversity and management of the Madrean Archipelago: The sky islands of southwestern United States and northwestern Mexico: Proceedings of the conference, Tucson, AZ. 19–23 Sept. 1994. Gen. Tech. Rep. RM-GTR-264. US For. Serv., Rocky Mtn. For. Range Exp. Stn., Fort Collins, CO.

Dennison, P.E., S.C. Brewer, J.D. Arnold, and M.A. Moritz. 2014. Large wildfire trends in the western United States, 1984–2011. Geophys. Res. Lett. 41:2928–2933. doi:10.1002/2014GL059576

Dickinson, W.R., 1992. Geologic map of Catalina core complex and San Pedro trough. Contrib. Map CM-92-C. Arizona Geo. Surv., Tucson.

Gutierrez-Jurado, H.A., and E.R. Vivoni. 2013. Ecogeomorphic expressions of an aspect-controlled semiarid basin: II. Topographic and vegetation controls on solar irradiance. Ecohydrology 6:24–37. doi:10.1002/eco.1263

Haith, D.A., and L.L. Shoemaker. 1987. Generalized watershed loading functions for stream-flow nutrients. Water Resour. Bull. 23:471–478. doi:10.1111/j.1752-1688.1987.tb00825.x

Hamon, W.R. 1961. Estimating potential evapotranspiration. Proc. Am. Soc. Civ. Eng. 87:107–120.

Heidbuchel, I., P.A. Troch, and S.W. Lyon. 2013. Separating physical and meteorological controls of variable transit times in zero-order catchments. Water Resour. Res. 49:7644–7657. doi:10.1002/2012WR013149

Holden, Z.A., C.H. Luce, M.A. Crimmins, and P. Morgan. 2012. Wildfire extent and severity correlated with annual streamflow distribution and timing in the Pacific Northwest, USA (1984–2005). Ecohydrology 5:677–684. doi:10.1002/eco.257

Holleran, M.E. 2013. Quantifying catchment scale soil variability in Marshall Gulch, Santa Catalina Mountains Critical Zone Observatory. M.S. thesis. Univ. of Arizona, Tucson.

Holleran, M., M. Levi, and C. Rasmussen. 2014. Quantifying soil and critical zone variability in a forested catchment through digital soil mapping. SOIL Discuss. 1:1–49. doi:10.5194/soild-1-1-2014

Huete, A., C. Justice, and H. Liu. 1994. Development of vegetation and soil indexes for MODIS-EOS. Remote Sens. Environ. 49:224–234. doi:10.1016/0034-4257(94)90018-3

Jenny, H. 1941. Factors of soil formation: A system of quantitative pedology. McGraw-Hill Book Co., New York.

Keith, H., B.G. Mackey, and D.B. Lindenmayer. 2009. Re-evaluation of forest biomass carbon stocks and lessons from the world's most carbon-dense forests. Proc. Natl. Acad. Sci. 106:11635–11640. doi:10.1073/pnas.0901970106

Kelliher, F.M., R. Leuning, M.R. Raupach, and E.D. Schulze. 1995. Maximum conductances for evaporation from global vegetation types. Agric. For. Meteorol. 73:1–16. doi:10.1016/0168-1923(94)02178-M

Lefsky, M.A., W.B. Cohen, S.A. Acker, G.G. Parker, T.A. Spies, and D. Harding. 1999. Lidar remote sensing of the canopy structure and biophysical properties of Douglas-fir western hemlock forests. Remote Sens. Environ. 70:339–361. doi:10.1016/S0034-4257(99)00052-8

Lieth, H. 1975. Primary production of the major vegetation units of the world. In: H. Lieth and R.H. Whittaker, editors, Primary productivity of the biosphere. Ecol. Stud. 14. Springer-Verlag, New York. p. 203–215.

Littell, J.S., D. McKenzie, D.L. Peterson, and A.L. Westerling. 2009. Climate and wildfire area burned in western U.S. ecoprovinces, 1916–2003. Ecol. Appl. 19:1003–1021. doi:10.1890/07-1183.1

L'vovich, M.I. 1979. World water resources and their future. Engl. transl. Am. Geophys. Union, Washington, DC.

Lybrand, R.A., and C. Rasmussen. 2014. Linking soil element-mass-transfer to microscale mineral weathering across a semiarid environmental gradient. Chem. Geol. 381:26–39. doi:10.1016/j.chemgeo.2014.04.022

Lybrand, R., C. Rasmussen, A. Jardine, P. Troch, and J. Chorover. 2011. The effects of climate and landscape position on chemical denudation and mineral transformation in the Santa Catalina Mountain Critical Zone Observatory. Appl. Geochem. 26:S80–S84. doi:10.1016/j.apgeochem.2011.03.036

Magirl, C.S., R.H. Webb, P.G. Griffiths, M. Schaffner, C. Shoemaker, E. Pytlak, et al. 2007. Impact of recent extreme Arizona storms. Eos Trans. AGU 88(17):191–193. doi:10.1029/2007EO170003

Mascaro, J., M. Detto, G.P. Asner, and H.C. Muller-Landau. 2011. Evaluating uncertainty in mapping forest carbon with airborne LiDAR. Remote Sens. Environ. 115:3770–3774. doi:10.1016/j.rse.2011.07.019

Melton, M.A. 1960. Intravalley variation in slope angles related to microclimate and erosional environment. Geol. Soc. Am. Bull. 71:133–144. doi:10.1130/0016-7606(1960)71[133:IVISAR]2.0.CO;2

Milligan, G.W. 1979. Ultrametric hierarchical clustering algorithms. Psychometrika 44:343–346. doi:10.1007/BF02294699

Minasny, B., A.B. McBratney, and S. Salvador-Blanes. 2008. Quantitative models for pedogenesis: A review. Geoderma 144:140–157. doi:10.1016/j.geoderma.2007.12.013

Moore, I.D., P.E. Gessler, G.A. Nielsen, and G.A. Peterson. 1993. Soil attribute prediction using terrain analysis. Soil Sci. Soc. Am. J. 57:443–452. doi:10.2136/sssaj1993.03615995005700020026x

National Research Council. 2010. Landscapes on the edge: New horizons for research on Earth's surface. Natl. Acad. Press, Washington, DC.

Niering, W.A., and C.H. Lowe. 1984. Vegetation of the Santa Catalina Mountains: Community types and dynamics. Vegetatio 58:3–28.

Pelletier, J.D., G.A. Barron-Gafford, D.D. Breshears, P.D. Brooks, J. Chorover, M. Durcik, et al. 2013. Coevolution of nonlinear trends in vegetation, soils, and topography with elevation and slope aspect: A case study in the sky islands of southern Arizona. J. Geophys. Res. Earth Surf. 118:741–758. doi:10.1002/jgrf.20046

Pelletier, J.D., and C. Rasmussen. 2009. Geomorphically based predictive mapping of soil thickness in upland watersheds. Water Resour. Res. 45:W09417. doi:10.1029/2008WR007319

Phillips, J.D. 2009. Biological energy in landscape evolution. Am. J. Sci. 309:271–289. doi:10.2475/04.2009.01

Poulos, M.J., J.L. Pierce, A.N. Flores, and S.G. Benner. 2010. Microclimate influences on slope angles in the western US. Geochim. Cosmochim. Acta 74:A827–A827.

Poulos, M.J., J.L. Pierce, A.N. Flores, and S.G. Benner. 2012. Hillslope asymmetry maps reveal widespread, multi-scale organization. Geophys. Res. Lett. 39:L06406. doi:10.1029/2012GL051283

Qi, J., Y.H. Kerr, M.S. Moran, M. Weltz, A.R. Huete, S. Sorooshian, and R. Bryant. 2000. Leaf area index estimates using remotely sensed data and BRDF models in a semiarid region. Remote Sens. Environ. 73:18–30. doi:10.1016/S0034-4257(99)00113-3

Rasmussen, C. 2012. Thermodynamic constraints on effective energy and mass transfer and catchment function. Hydrol. Earth Syst. Sci. 16:725–739. doi:10.5194/hess-16-725-2012

Rasmussen, C., and E.L. Gallo. 2013. A comparison of model and empirical measures of catchment-scale effective energy and mass transfer. Hydrol. Earth Syst. Sci. 17:3389–3395. doi:10.5194/hess-17-3389-2013

Rasmussen, C., R.J. Southard, and W.R. Horwath. 2005. Modeling energy inputs to predict pedogenic environments using regional environmental databases. Soil Sci. Soc. Am. J. 69:1266–1274. doi:10.2136/sssaj2003.0283

Rasmussen, C., and N.J. Tabor. 2007. Applying a quantitative pedogenic energy model across a range of environmental gradients. Soil Sci. Soc. Am. J. 71:1719–1729. doi:10.2136/sssaj2007.0051

Rasmussen, C., P.A. Troch, J. Chorover, P. Brooks, J. Pelletier, and T.E. Huxman. 2011. An open system framework for integrating critical zone structure and function. Biogeochemistry 102:15–29. doi:10.1007/s10533-010-9476-8

Schulze, E.D., F.M. Kelliher, C. Korner, J. Lloyd, and R. Leuning. 1994. Relationships among maximum stomatal conductance, ecosystem surface conductance, carbon assimilation rate, and plant nitrogen nutrition: A global ecology scaling exercise. Annu. Rev. Ecol. Syst. 25:629. doi:10.1146/annurev.es.25.110194.003213

Shuttleworth, W.J. 1993. Evaporation. In: D.R. Maidment, editor, Handbook of hydrology. McGraw-Hill, New York. p. 4.1–4.53.

Smith, T.M., H.H. Shugart, and F.I. Woodward. 1997. Plant functional types: Their relevance to ecosystem properties and global change. Int. Geosphere–Biosphere Progr. Book Ser. Cambridge Univ. Press, Cambridge, UK.

Swetnam, T.L. 2013. Cordilleran forest scaling dynamics and disturbance regimes quantified by aerial LiDAR. Ph.D. diss. Univ. of Arizona, Tucson.

Tarboton, D.G., R.L. Bras, and I. Rodriguez-Iturbe. 1991. On the extraction of channel networks from digital elevation data. Hydrol. Processes 5:81–100. doi:10.1002/hyp.3360050107

Thornthwaite, C.W., and J.R. Mather. 1957. Instructions and tables for computing potential evapotranspiration and the water balance. Publ. Climatol. Vol. 10, no. 3. Drexel Inst. Technol., Lab. Climatol., Centerton, NJ

Volobuyev, V.R. 1964. Ecology of soils. Acad. Sci. Azerbaidzn SSR, Ins. Soil Sci. Agrochem., Israel Progr. Sci. Transl., Jersualem.

Walther, G.R., E. Post, P. Convey, A. Menzel, C. Parmesan, T.J.C. Beebee, et al. 2002. Ecological responses to recent climate change. Nature 416:389–395. doi:10.1038/416389a

Westerling, A.L., A. Gershunov, T.J. Brown, D.R. Cayan, and M.D. Dettinger. 2003. Climate and wildfire in the western United States. Bull. Am. Meteorol. Soc. 84:595. doi:10.1175/BAMS-84-5-595

Whittaker, R.H., S.W. Buol, W.A. Niering, and Y.H. Havens. 1968. A soil and vegetation pattern in the Santa Catalina Mountains, Arizona. Soil Sci. 105:440–451. doi:10.1097/00010694-196806000-00010

Whittaker, R.H., and W.A. Niering. 1975. Vegetation of the Santa Catalina Mountains, Arizona: V. Biomass, production, and diversity along the elevation gradient. Ecology 56:771–790. doi:10.2307/1936291

Zhang, L., W.R. Dawes, and G.R. Walker. 2001. Response of mean annual evapotranspiration to vegetation changes at catchment scale. Water Resour. Res. 37:701–708. doi:10.1029/2000WR900325

Zhang, L., K. Hickel, W.R. Dawes, F.H.S. Chiew, A.W. Western, and P.R. Briggs. 2004. A rational function approach for estimating mean annual evapotranspiration. Water Resour. Res. 40:W02502. doi:10.1029/2003WR002710

Zhang, Y., H. Wei, and M.A. Nearing. 2011. Effects of antecedent soil moisture on runoff modeling in small semiarid watersheds of southeastern Arizona. Hydrol. Earth Syst. Sci. 15:3171–3179. doi:10.5194/hess-15-3171-2011